

pubs.acs.org/cm Article

# Carbonate Formation during Nickel Hydroxide Precipitation **Reduces Pseudocapacitive Performance**

Published as part of Chemistry of Materials special issue "Operando and In Situ Characterization of Energy Storage Materials".

Anja Siher, Ksenija Maver, Iztok Arčon, and Andraž Mavrič\*



Cite This: Chem. Mater. 2025, 37, 7813-7822



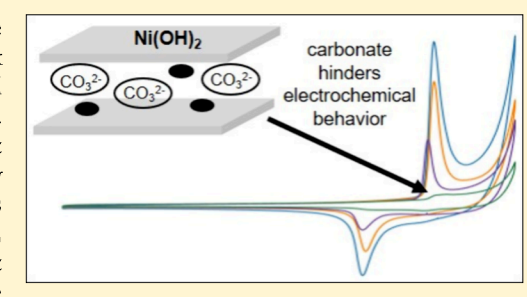
ACCESS |

Metrics & More

Article Recommendations

Supporting Information

ABSTRACT: Nickel hydroxide  $(Ni(OH)_2)$  is a promising pseudocapacitive material owing to its high theoretical capacitance and reversible Ni<sup>2+</sup>/Ni<sup>3+</sup> redox activity. Here we demonstrate that carbonate incorporation during hydrothermal synthesis is the key structural factor limiting its electrochemical performance. Ni(OH)<sub>2</sub> was prepared using hexamethylenetetramine (HMT) and urea at different synthesis temperatures, and carbonate incorporation was quantified by XRD, FTIR, Raman, TGA-MS, and CaCO<sub>3</sub> precipitation. HMT-derived samples at a low temperature (80 °C) formed a turbostratic  $\alpha$ -phase with interlayer water, delivering the highest specific capacitance (~870 F g<sup>-1</sup> at 1 A g<sup>-1</sup>) and excellent cycling stability (92-96% retention after 1000 cycles). In contrast, increasing the



synthesis temperature promoted carbonate incorporation and crystallization into nickel carbonate hydroxide, reducing the interlayer spacing and surface area and increasing charge-transfer resistance. Urea-derived samples incorporated carbonate at all synthesis temperatures, yielding phases with capacitances an order of magnitude lower than those of HMT analogues. Electrochemical impedance spectroscopy confirmed that carbonate incorporation blocks redox-active sites and hinders ion/electron transport. These results provide a quantitative mechanistic understanding of how carbonate formation governs transition metal layered hydroxide performance, establishing guidelines for optimizing hydrothermal synthesis of pseudocapacitive electrodes.

## 1. INTRODUCTION

Among transition metal hydroxides for pseudocapacitive applications, nickel hydroxide (Ni(OH)<sub>2</sub>) has been widely explored as an electrode material. Its high theoretical specific capacitance arises from the reversible Ni<sup>2+</sup>/Ni<sup>3+</sup> redox couple and a layered structure that enables ion intercalation. In practice, Ni(OH)<sub>2</sub> is most often used as a battery-type positive electrode in hybrid (asymmetric) supercapacitor architectures paired with a capacitive negative electrode (e.g., activated carbon). This device architecture combines faradic and doublelayer electrodes to extend the operating voltage, boost energy density, and retain high power and cycling stability.<sup>1-4</sup> To expose redox-active sites, extensive efforts have been made to optimize the Ni(OH)<sub>2</sub> structure through different synthesis methods. 5,6 Nickel hydroxide exists in two polymorphs,  $\alpha$ -Ni(OH)<sub>2</sub> and  $\beta$ -Ni(OH)<sub>2</sub>, both consisting of layers of edgesharing Ni(OH)<sub>6</sub> octahedra. Both phases belong to hexagonal crystal family with Ni(OH)<sub>2</sub> layers stacked along the c-axis. In brucite-like  $\beta$ -Ni(OH)<sub>2</sub>, the metal hydroxide layers are stacked together with a minimal interlayer distance.  $\alpha$ -Ni(OH)<sub>2</sub> exhibits a hydrotalcite-like structure, where positively charged  $Ni(OH)_{2-x}$  layers are intercalated with anions and water molecules. The turbostratic nature of  $\alpha$ -Ni(OH) $_2$  results in greater structural disorder, more flexible interlayer spacing, and

improved accessibility to redox-active sites, often leading to superior pseudocapacitive performance compared to that of the  $\beta$ -phase.<sup>7,8</sup> The structure and morphology of  $\alpha$ -Ni(OH)<sub>2</sub> can be tailored by introducing various molecules and anions into the interlayer space, whereas  $\beta$ -Ni(OH)<sub>2</sub>, with its brucitelike structure, does not accommodate guest species. 9,10 Under strongly alkaline conditions,  $\alpha$ -Ni(OH)<sub>2</sub> recrystallizes to the  $\beta$ -Ni(OH)<sub>2</sub> phase. Hydrothermal synthesis is one of the most commonly employed approaches for Ni(OH)<sub>2</sub> preparation due to its simplicity and effectiveness in controlling particle size and shape.<sup>6</sup> This method can produce a wide range of morphologies and structures, such as nanoplate-like, flowerlike, nanotubes, nanospheres, and nanorods. Among these the flower-like morphology attracts particular attention for electrochemical applications because of high electrolyte-accessible surface area.11

Received: June 11, 2025 Revised: August 22, 2025 Accepted: September 19, 2025 Published: September 25, 2025





The Ni(OH)<sub>2</sub> particles are in general synthesized by precipitation from an aqueous solution of Ni<sup>2+</sup> salts using a hydrothermal method, where the source of hydroxide is generated in situ via slow hydrothermal decomposition of an organic precursor such as urea or HMT. The gradual release of ammonia during decomposition allows controlled precipitation that helps in particle ripening, often leading to improved crystallinity, size, and morphology. 12 Both urea and HMT ultimately yield ammonia and CO2; HMT decomposes through a two-step mineralization process, involving formate and ammonia formation in the first step, 13 requiring a higher temperature for subsequent CO<sub>2</sub> formation. These different decomposition pathways and temperature sensitivity influence the incorporation of carbonate into the layered structure, which, in turn, can modify electrochemical performance. While previous studies have investigated HMT-derived Ni(OH)2, particularly in terms of morphology, 9,14 we have recently shown for cobalt hydroxide that the temperature of HMT decomposition critically affects the crystal structure, with direct consequences for capacitance. To clarify the role of carbonate formation in Ni(OH)<sub>2</sub> prepared by hydrothermal precipitation, we prepared powders using urea (Ni(OH)2-U) and hexamethylenetetramine (Ni(OH)2-H) as hydroxide sources at different temperatures and examined their structural, morphological, and electrochemical characteristics. As confirmed by previously reported data summarized in Table S1, support materials can strongly influence measured capacitance values; however, direct comparison of the structurecapacitance relationship across literature reports is problematic due to the frequent use of redox-active substrates such as Ni foam, which contribute additional faradic charge. Here, alongside electrochemical measurements, we employed in situ Ni K-edge X-ray absorption spectroscopy (XAS) on the bestperforming sample to probe the redox behavior of Ni<sup>2+</sup> cations under electrochemical conditions.

# 2. EXPERIMENTAL SECTION

- **2.1. Materials.** Ni(NO $_3$ ) $_2$ ·6H $_2$ O (98%), hexamethylenetetramine ( $\geq$ 99.0%), and a Nafion 117-containing solution (5 wt % in a mixture of lower aliphatic alcohols and water) were purchased from Sigma-Aldrich. Urea ( $\geq$ 98%) was purchased from Alfa Aesar. We used carbon paper as the substrate for the electrodes (Avcarb GDS2230). The electrolyte was prepared using potassium hydroxide (85%) purchased from Thermo Scientific Chemicals.
- **2.2. Synthesis of Ni(OH)**<sub>2</sub>. The Ni(OH)<sub>2</sub> particles were prepared through hydrothermal synthesis by dissolving (a) 2 mmol of Ni(NO<sub>3</sub>)<sub>2</sub>·6H<sub>2</sub>O and 10 mmol of HMT in 20 mL of deionized water and (b) 2 mmol of Ni(NO<sub>3</sub>)<sub>2</sub>·6H<sub>2</sub>O and 20 mmol of urea in 20 mL of deionized water. The solution was first stirred for 30 min and then transferred to an autoclave. The samples were prepared at different temperatures and time durations: 80 °C (for 48 h), 100 °C (for 48 h), 120 °C (for 24 h), and 140 °C (for 24 h). Longer durations were applied at lower synthesis temperatures to compensate for reduced precipitation rates and ensure a sufficient product yield. After the synthesis, the solution was cooled to room temperature. The resulting precipitate was thoroughly washed with deionized water.
- **2.3. Preparation of the Electrodes.** A suspension of Ni(OH)<sub>2</sub> was prepared by mixing a powder of Ni(OH)<sub>2</sub> particles with ethanol and a Nafion solution, followed by agitation for 1 h in an ultrasound bath to prepare a 1 mg mL<sup>-1</sup> suspension of Ni(OH)<sub>2</sub>, with 0.1 wt % Nafion. Precisely, 10  $\mu$ L of the suspension was deposited onto the acetone-cleaned carbon paper for a final loading of 50  $\mu$ g cm<sup>-2</sup>.
- **2.4. Characterization.** The surface morphology of the particles was investigated using a SEM JSM7001TTLS instrument (JEOL, Japan) at 15 keV and a TEM JEM2100F instrument (JEOL, Japan) at 200 keV. The X-ray diffractograms were measured using SmartLab SE

(Rigaku Corp., Japan) using a Cu radiation source (Cu Kα, 0.1541 mm) from  $8^{\circ}$  to  $80^{\circ}$  with a step of  $0.01^{\circ}$  and a speed of  $5^{\circ}/\text{min}$ . Fourier transform infrared (FTIR) spectroscopy was performed using a Spectrum100 instrument (PerkinElmer, USA) with an ATR attachment (PIKE, USA) averaging over 16 scans in the wavenumber range from 4000 to 450 cm<sup>-1</sup> with a resolution of 4 cm<sup>-1</sup>. Raman spectra were obtained by focusing a 532 nm laser (50 mW Cobot 80-DPL, Sweden) on the pressed powder sample using a Raman microscope (A.P.E. Research Nanotechnology, Italy). The Raman signal was collected via optical fiber and measured using an SCT320 IsoPlane spectrophotometer equipped with a CCD camera (Teledyne Princeton Instruments, USA) and a high-resolution grating (1800 grooves mm<sup>-1</sup>). Spectra are given as an average of two spectra each with an acquisition time of 20 s. Thermogravimetric measurements were performed using a TGA/DSC2 instrument (Mettler Toledo, Switzerland) coupled with gas analyzer Omnistar GSD (Pfeiffer Vacuum, Germany) over the temperature range of 40-600 °C, with a heating rate of 10 °C min<sup>-1</sup> in a static air atmosphere. Using a high vacuum physisorption analyzer Autosorb iQ (Anton Paar, USA), the nitrogen adsorption and desorption isotherms were measured after the outgassing under vacuum at 80 °C for 6 h. The specific surface area was calculated by the Brunauer-Emmet-Teller (BET) method, and the pore size distribution was determined from the isotherms using a DFT model.

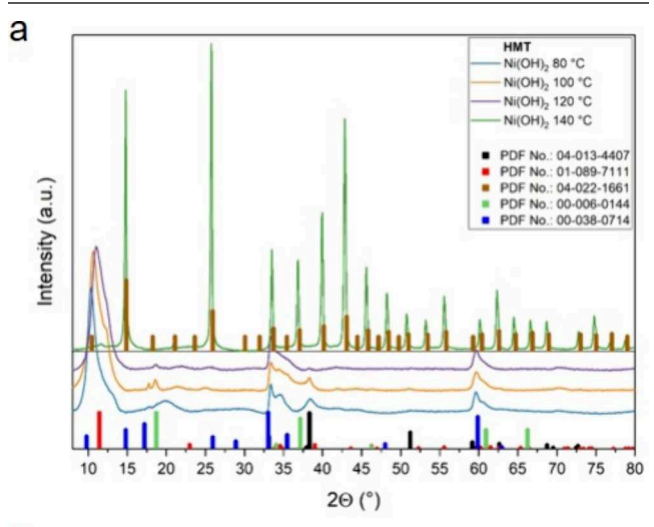
Electrochemical measurements were conducted using a three-electrode Swagelok electrochemical cell (S4R, France) and an electrochemical workstation SP-300 (Biologic, France) with the EC-Lab software package. A Ag/AgCl double-junction electrode in a 3.8 M KCl solution was used as the reference electrode, and Pt-coated carbon was used as the counter electrode. All electrochemical measurements were performed using an aqueous solution of N<sub>2</sub>-purged 1 M KOH as an electrolyte with a pH of 13.9. We performed cyclic voltammetry (CV), galvanostatic charge—discharge (GCD) tests, and electrochemical impedance spectroscopy (EIS). EIS measurements were performed at 1.40 V versus RHE with an AC perturbation amplitude of 10 mV over a frequency range from 100 kHz to 10 mHz and fitted using EC-Lab software.

In situ XAS was conducted on a P65 beamline at PETRA III (DESY, Hamburg, Germany). A Si(111) double-crystal monochromator was used with an energy resolution of about 1 eV at 8 keV. The beam size on the sample was 0.3 mm × 1 mm. Higher-order harmonics were effectively eliminated by a flat mirror. Three repetitions of XAS spectra were measured in continuous detection mode in short 3 min scans at each potential step during the in situ experiment at different applied potentials in charging and discharging directions for Ni(OH)2-H prepared at 80 °C. The intensity of the monochromatic X-ray beam was measured with the ionization detectors (I1, I2, and I3) filled with 1020 mbar of suitable absorption gas mixtures to absorb a total of 16% (10% Ar, 90%  $N_2$ ), 54% (15% Ar, 85%  $N_2$ ), and 90% (Kr), respectively. The absorption spectra were measured in the energy region from -150 to 1000 eV relative to the Ni K edge (8333 eV). The exact energy calibration was established with absorption measurements on a 5  $\mu$ m thick Ni metal foil placed between the second (I2) and third (I3) ionization detectors. The absolute energy reproducibility of the measured spectra was  $\pm 0.05$  eV. Reference compounds LiNiO2, NiO, and as-prepared Ni(OH)2-H prepared at 80 °C were homogeneously mixed with 50 mg of boron nitride and prepared in the form of homogeneous pellets with an optimal total absorption thickness of about 1.5 above the Ni K edge. The pellets and the three-electrode electrochemical cell for in situ measurements were placed in the monochromatic beam after the first (I1) ionization detector. The electrochemical cell was tilted 45° to the X-ray beam for fluorescence measurements. The fluorescence signal was detected with a Passivated Implanted Planar Silicon (PIPS) detector. The main electrochemical three-electrode compartment was confined by two Kapton foils, which serve as windows for the Xray beam. A Ag/AgCl (3.8 M KCl) double-junction electrode was used as the reference electrode, and 20 nm of Pt on carbon paper was used as the counter electrode. The 1 M KOH electrolyte was constrained in 0.5 mm of cellulose paper. The potentials were applied

using a model VMP-300 potentiostat (BioLogic). XAS spectra were analyzed with DEMETER (IFEFFIT). <sup>16</sup>

## 3. RESULTS AND DISCUSSION

**3.1. Structure and Morphology.** The structural evolution of  $Ni(OH)_2$  strongly depends on the synthesis temperature and the choice of the organic precursor. XRD and Raman analyses reveal that the HMT-derived samples (Figure 1a)



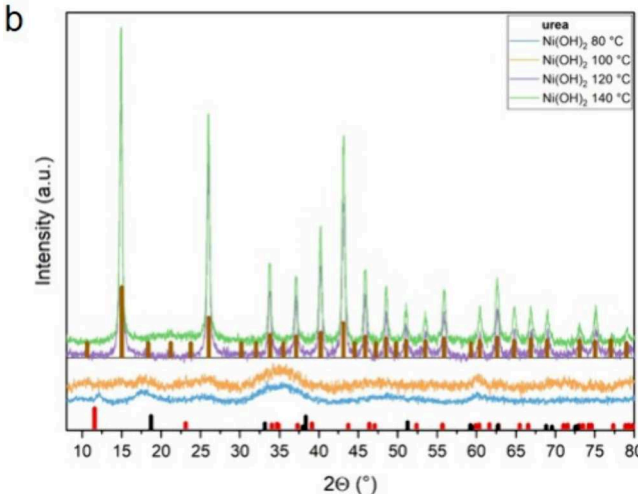


**Figure 1.** X-ray diffraction patterns of (a) Ni(OH)<sub>2</sub>-H and (b) Ni(OH)<sub>2</sub>-U samples synthesized at 80, 100, 120, and 140 °C. The corresponding reference patterns are  $\beta$ -Ni(OH)<sub>2</sub> (PDF Card 04-013-4407),  $\alpha$ -Ni(OH)<sub>2</sub> (jamborite, PDF Card 01-089-7111), nickel oxide carbonate hydroxide (PDF Card 04-022-1661), nickel oxide hydroxide (PDF Card 00-006-0144), and nickel carbonate hydroxide hydrate (PDF Card 00-038-0714). Colors in the figure correspond to synthesis temperatures for samples and to specific reference phases, as indicated in the legend.

prepared at 80–120 °C are dominated by the  $\alpha$ -Ni(OH)<sub>2</sub> phase (jamborite, PDF Card 01-089-7111, red),<sup>17</sup> with the (003) reflection near 11° displaying two contributions: a sharper peak at ~11.5° ( $d \approx 7.7$  Å) corresponding to the carbonate-intercalated  $\alpha$ -phase and a broader, lower-2 $\theta$  shoulder that shifts progressively from 11.38° ( $d \approx 7.8$  Å at 120 °C) to 10.69° ( $d \approx 8.2$  Å at 100 °C) and further to 10.36° ( $d \approx 8.5$  Å at 80 °C), indicating the largest layer expansion at the lowest synthesis temperature. The relative contribution of these two components, expressed as the ratio of the integrated

peak intensity of the HMT residue shoulder to the carbonate peak, decreases from 3.3 for the 80 °C sample to 2.4 at 100 °C and further to 0.5 at 120 °C, confirming the progressive conversion of residual HMT into carbonate at higher synthesis temperatures. At 140 °C, the material transforms completely into crystalline nickel oxide carbonate hydroxide (PDF Card 04-022-1661, brown). The urea-derived samples (Figure 1b) show broader reflections and poor crystallinity at 80–100 °C, but already at 120–140 °C, they crystallize into the carbonate hydroxide phase, highlighting that urea decomposition accelerates carbonate incorporation compared with HMT.

Raman spectra (Figures S1 and S2) support this structural evolution and provide additional insight into local bonding. In the HMT series, two low-frequency modes (Figures S1a) are consistently observed: the Ni-OH stretching vibration near 400 cm<sup>-1</sup> and the Ni-O vibration around 500 cm<sup>-1</sup>, both characteristic of layered nickel hydroxides.<sup>19</sup> The carbonate symmetric stretch (Figures S1b) is evident at ~1040 cm<sup>-1</sup> in the 80-120 °C samples, confirming the presence of carbonate species, and shifts to ~1112 cm<sup>-1</sup> in the 140 °C sample. This shift reflects the increased bond strength, indicating that carbonate becomes more strongly incorporated into the crystal lattice at higher temperatures.<sup>20</sup> In the urea-derived series, similar Ni-OH ( $\sim$ 400 cm<sup>-1</sup>) and Ni-O ( $\sim$ 530 cm<sup>-1</sup>) vibrations (Figures S2a) are observed for all samples and become more pronounced for the more crystalline samples prepared at 120 and 140 °C. The carbonate symmetric stretch (Figure S2b) appears at  $\sim 1070$  cm<sup>-1</sup> in the 80–100 °C samples but shifts to  $\sim$ 1111 cm<sup>-1</sup> at 120–140 °C, mirroring the behavior of the HMT-derived series and confirming that urea synthesis produces strongly bonded carbonate even at lower temperatures.

The extent and nature of carbonate incorporation are further supported by thermal analysis and vibrational spectroscopy. TGA-MS of HMT-derived samples (Figure S3a-c) shows sharp dehydroxylation steps with H<sub>2</sub>O and CO<sub>2</sub> release near 340 °C for samples prepared at 80-120 °C but broadens into two distinct peaks (~325 and 400 °C) for samples prepared at 140 °C (Figure S3d), characteristic of carbonate hydroxide decomposition.<sup>21</sup> In contrast, urea-derived samples exhibit this two-step decomposition already at 80–100 °C (Figure S4a,b), indicating earlier and more extensive carbonate incorporation. This behavior is consistent with carbonate-intercalated double hydroxides, where the decomposition step is split into partial dehydroxylation of hydroxide layers and decarboxylation, followed by complete dehydroxylation.<sup>22</sup> This observation is further supported by the MS curves, which show the release of  $\rm H_2O~(\it m/z~18)$  and  $\rm CO_2~(\it m/z~44)$  during each displaying two distinct peaks within the same thermal event. Notably, this two-step process was not observed in the Ni(OH)<sub>2</sub>-H samples at lower temperatures. FTIR spectra confirm this trend (Figures S5 and S6). In the HMT series, broad absorptions in the range of 2800–3000 cm<sup>-1</sup> (Figure S5a) are observed for all samples and are attributed to C-H stretching vibrations, consistent with residual organic species from incomplete HMT decomposition. A strong band at ~1635 cm<sup>-1</sup> appears in the 80–120 °C samples and corresponds to the bending mode of interlayer or adsorbed water, confirming the presence of a hydrated layered structure capable of hosting intercalated species. The intensity of this band diminishes drastically in the 140 °C sample, indicating the loss of interlayer water and the collapse of the gallery structure as the carbonate hydroxide phase crystallizes. The carbonate-related absorptions (Figure

S5b) are weak or absent at 80-100 °C; however, at 120 °C a shoulder near 1350 cm  $^{-1}$  appears, while at 140  $^{\circ}$ C, the  $\nu_3$ asymmetric stretch of carbonate becomes a broad, intense band spanning the range of 1600-1300 cm<sup>-1</sup> with clear splitting into multiple components. This splitting reflects different coordination geometries of the intercalated carbonate. The  $\nu_2$  out-of-plane bending mode at ~850 cm<sup>-1</sup> emerges only in the 140 °C sample, confirming the presence of strongly lattice-bonded carbonate. <sup>23,24</sup> In the urea series (Figure S6), carbonate features are visible at all temperatures. A broad band at 1600-1300 cm<sup>-1</sup> sharpens and splits progressively from 80 to 140 °C, while the  $\nu_2$  bending mode near 850 cm<sup>-1</sup> is consistently observed, becoming most intense at 140 °C. The intensity growth and band splitting with temperature demonstrate both an increasing concentration and stronger incorporation of carbonate into the hydroxide framework. Unlike the HMT series, the water bending band at ~1635 cm<sup>-1</sup> is weak or absent across the urea samples, demonstrating that interlayer water is largely missing and that the layered structure is never well developed. Instead, carbonate ions dominate the interlayer environment, even at low temperatures, producing compact carbonate hydroxide structures with limited ion-accessible galleries. To complement the thermal decomposition and spectroscopic evidence, the formation of carbonate during hydrothermal decomposition of HMT and urea was directly quantified using CaCl2 as a selective carbonate precipitating agent (see the Supporting Information for details). The hydrothermal decomposition solutions of HMT and urea (prepared without Ni<sup>2+</sup>) were reacted with Ca<sup>2+</sup>, and the resulting CaCO<sub>3</sub> precipitate was isolated and weighed (Table S2). For HMT, the level of carbonate formation remains low at 80-120 °C (0.09-0.20 g) and becomes significant only at 140 °C (0.43 g). In contrast, urea decomposition generates much larger amounts of carbonate, increasing from 0.14 g at 80 °C to 0.43 g at 100 °C, and exceeding 1.15 g at 120-140 °C. These results confirm that carbonate incorporation is strongly temperature-dependent and far more pronounced in the urea series, in agreement with the TGA-MS and FTIR analyses.

The incorporation of carbonate directly influences morphology and porosity. SEM and TEM images (Figure 2) show that HMT-derived samples at 80-120 °C consist of thin nanosheets assembled into flower-like clusters (a few micrometers in size), whereas at 140 °C, these collapse into compact agglomerates (Figure 2d,h). Urea-derived powders (Figure 3) display sheet-based microsphere agglomerates at 80-100 °C, evolving into compact spheres by 120-140 °C. In parallel, BET analysis further reflects the morphological and structural transitions. The BET surface areas of HMT-derived samples decrease systematically from 368 m $^2$  g $^{-1}$  at 80  $^{\circ}$ C to only 81 m<sup>2</sup> g<sup>-1</sup> at 140 °C (Table S3). A similar trend is observed for the urea-derived series, although at consistently lower values, in agreement with their denser, carbonate-rich structures. The pore size distribution (Figures S7 and S8), obtained by DFT analysis of the adsorption-desorption isotherms, highlights clear differences between the two series. In the HMT samples, the 80 °C powder contains a large fraction of micropores, consistent with its nanosheet-based morphology and expanded interlayer galleries. With an increase in the synthesis temperature to 120 °C, the proportion of micropores decreases while mesopores become dominant, reflecting reduced interlayer spacing. By 140 °C, the HMT product is essentially mesoporous with very few micropores, correlating with the

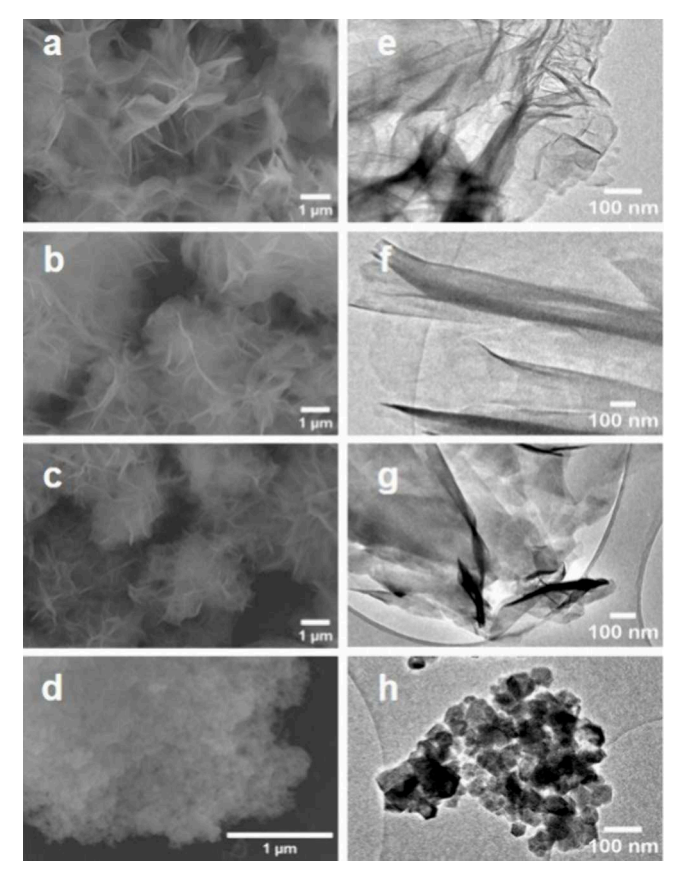


**Figure 2.** SEM (left) images of Ni(OH)<sub>2</sub>-H particles synthesized using HMT at (a) 80, (b) 100, (c) 120, and (d) 140 °C and TEM (right) images of Ni(OH)<sub>2</sub>-H particles prepared at (e) 80, (f) 100, (g) 120, and (h) 140 °C.

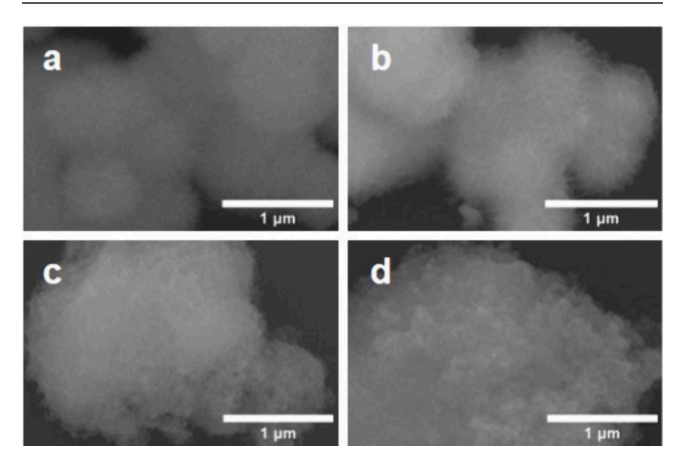
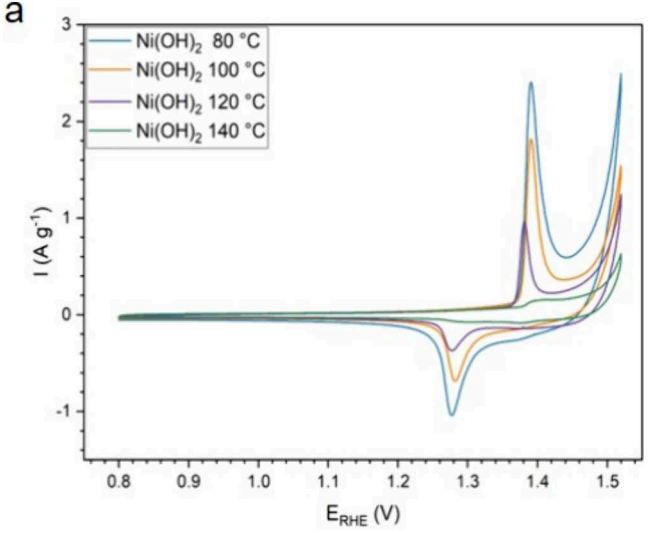
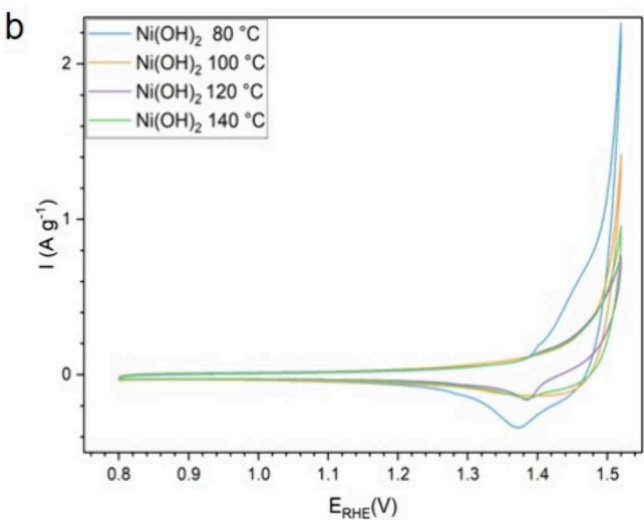


Figure 3. SEM images of  $Ni(OH)_2$ -U particles synthesized using urea at (a) 80, (b) 100, (c) 120, and (d) 140 °C.

compact agglomerates observed via SEM and TEM. The ureaderived powders show a different porosity profile. Even at 80 °C the isotherms are dominated by mesopores and lack a significant micropore contribution, consistent with the weak or absent interlayer water identified by FTIR.

**3.2. Electrochemical Performance.** Cyclic voltammetry reveals that Ni(OH)<sub>2</sub>-H electrodes (Figure 4a) synthesized at 80–120 °C exhibit well-defined and reversible Ni<sup>2+</sup>/Ni<sup>3+</sup> redox processes, as evidenced by well-defined oxidation and reduction peaks characteristic of Ni(OH)<sub>2</sub>.<sup>7</sup> An oxidation





**Figure 4.** Cyclic voltammograms of (a)  $Ni(OH)_2$ -H and (b)  $Ni(OH)_2$ -U electrodes synthesized at 80, 100, 120, and 140  $^{\circ}$ C, recorded in 1 M KOH at a scan rate of 1 mV s<sup>-1</sup> over the potential range of 0.8–1.6 V vs RHE.

peak appears at  $\sim$ 1.39 V, attributed to the Ni<sup>2+</sup>/Ni<sup>3+</sup> transition, with the corresponding reduction peak at  $\sim$ 1.28 V. The highest current density and integrated charge are observed for the 80 °C sample, where the phase with the largest interlayer spacing  $(d \approx 8.5 \text{ Å})$  dominates, interlayer water is abundant, and the nanosheet morphology maximizes redox site accessibility. With an increase in synthesis temperature, the redox peaks gradually weaken, reflecting partial blocking of redox-active sites, which agrees with the increase in the carbonate concentration that is evident in XRD, Raman, and FTIR data. At 140 °C, the redox peaks are greatly diminished and appear at higher potentials, consistent with the collapse of the layered structure into crystalline carbonate hydroxide that limits electrolyte ion access. In the Ni(OH)<sub>2</sub>-U electrode series (Figure 4b), the redox peaks are already much weaker and shifted even at 80 °C, confirming earlier carbonate incorporation and the absence of hydrated interlayers. For the sample prepared at 80 °C, the oxidation peak appears at 1.41 V and the reduction peak at 1.38 V. Figure S9a shows a drastic decrease in current compared to that of the Ni(OH)2-H analogue at the same temperature. At higher synthesis temperatures, the CV profiles

of the Ni(OH)<sub>2</sub>-U electrodes become nearly featureless, dominated by nonfaradic charging with a minimal pseudocapacitive contribution.

Galvanostatic charge—discharge (GCD) measurements were performed at various current densities within the potential window of 0.8-1.46 V versus RHE. The charge-discharge profiles of the Ni(OH)2-H series (Figure 5a) display distinct plateaus, corresponding well to the oxidation and reduction features identified in the cyclic voltammograms, confirming a faradic charge-storage mechanism dominated by the Ni<sup>2+</sup>/Ni<sup>3+</sup> transition. In contrast, Ni(OH)2-U (Figure 5b) exhibits less pronounced plateaus, through redox contributions that are still evident, consistent with the weaker and shifted CV peaks of these samples. The potentials recorded in the chargedischarge curves align with those observed in the cyclic voltammograms. Among all of the samples, Ni(OH)2-H prepared at 80 °C exhibited the longest discharge time, reflecting its expanded layered structure, hydrated interlayers, and large BET surface area, which together maximize accessibility of redox-active Ni sites. In contrast, the Ni-(OH)<sub>2</sub>-H sample, synthesized at 140 °C, which adopts a nickel carbonate hydroxide structure, showed a drastically shorter discharge time due to collapse of the layered galleries and incorporation of carbonate, limiting electrolyte ion access. A similar deterioration of pseudocapacitance with carbonate incorporation has been reported for cobalt hydroxides upon crystallization into cobalt carbonate hydroxide hydrate. 15

The cycling stability (Figure 6) of the best-performing Ni(OH)2-H prepared at 80 °C was evaluated through repeated charge-discharge measurements, with capacitance retention (in percent) plotted against cycle number. The electrode retained 96% of its initial capacitance after 1000 cycles at 1 A g<sup>-1</sup>, indicating excellent long-term stability. Capacitance values, calculated from discharge times and operating potentials,<sup>2</sup> decreased progressively with an increase in synthesis temperature in the Ni(OH)<sub>2</sub>-H series (Figure 5b), 80  $^{\circ}$ C > 100  $^{\circ}$ C > 120 °C > 140 °C, in line with the gradual replacement of HMT residues by carbonate as confirmed by XRD, FTIR, and Raman analyses. This demonstrates that partial preservation of interlayer water and low carbonate content at ≤120 °C are critical to maintaining pseudocapacitive properties. Regardless of the synthesis temperature, all Ni(OH)<sub>2</sub>-U samples (Figure 5d) displayed capacitances at least an order of magnitude lower than those of their HMT-derived counterparts. Even at 80-100 °C, where these samples remain poorly crystalline, FTIR spectra confirm the presence of carbonate arising from urea decomposition. At 120-140 °C, crystallization into nickel carbonate hydroxide further suppresses electrochemical activity. Thus, carbonate incorporation, whether in crystalline form or within a disordered matrix, has a strongly negative effect on the electrochemical accessibility of the Ni2+ sites. Comparable behavior has been observed in NiFe-LDH electrocatalysts, where basal-plane carbonate intercalation severely degraded redox behavior.<sup>26</sup> A schematic diagram (Scheme 1 of the Supporting Information) summarizes the phase transformation at different synthesis temperatures (80, 100, 120, and 140 °C) for both HMT and urea, along with their corresponding electrochemical impact. The diagram shows that higher synthesis temperatures promote the formation of nickel carbonate hydroxide (HMT at 140 °C and urea at 120 and 140 °C), leading to reduced electrochemical performance as reflected in the capacitance values,

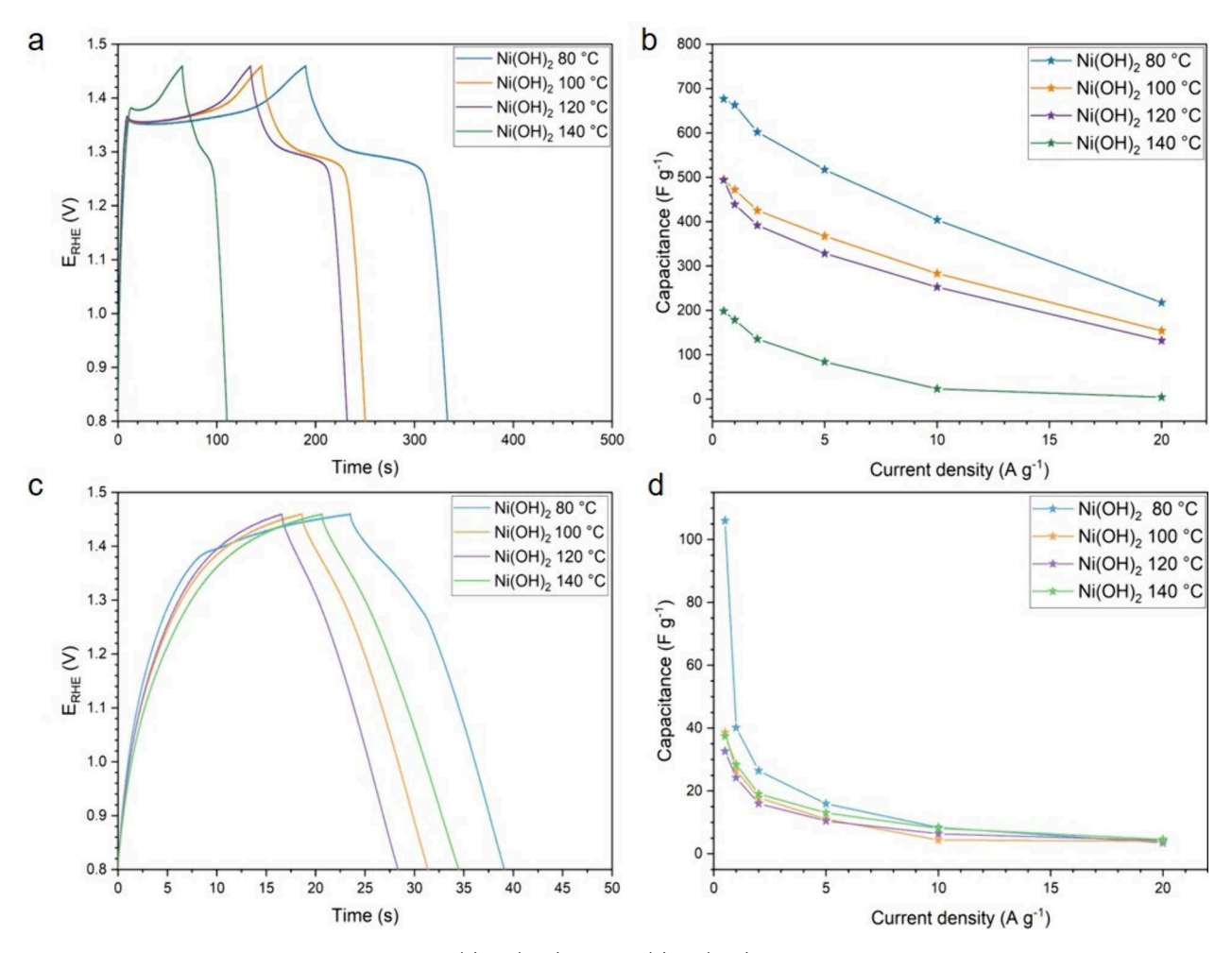


Figure 5. Galvanostatic charge—discharge curves for (a)  $Ni(OH)_2$ -H and (c)  $Ni(OH)_2$ -U electrodes synthesized at 80, 100, 120, and 140 °C, measured in 1 M KOH at a current density of 1 A g<sup>-1</sup>. The corresponding specific capacitances were calculated at different current densities for (b)  $Ni(OH)_2$ -H and (d)  $Ni(OH)_2$ -U.

thereby highlighting the relationship between structure and electrochemical accessibility.

To assess the kinetic behavior of the Ni(OH)<sub>2</sub>-H and Ni(OH)<sub>2</sub>-U samples synthesized at 80, 100, 120, and 140 °C, electrochemical impedance spectroscopy (EIS) measurements were performed. The corresponding Nyquist plots, along with the fitted equivalent circuit, are shown in Figures S10 and S11. The equivalent circuit consists of the series resistance ( $R_{\rm s}$ ), representing the overall ohmic resistance of the electrode–electrolyte system; a double-layer capacitance ( $C_{\rm dl}$ ); the charge-transfer resistance ( $R_{\rm ct}$ ) in parallel with a constant phase element (CPE) to account for nonideal capacitive behavior; and the Warburg element (W), representing ion diffusion within the electrode material. The best fit values are summarized in Tables S4 and S5.

Qualitatively, the Nyquist plots reveal notable differences between the two synthesis routes and temperatures. For the HMT series (Figure S10), the samples prepared at 80, 100, and 120 °C display well-defined semicircles, followed by a Warburg-type tail, indicative of a combined charge-transfer and diffusion process. <sup>27</sup> In contrast, the HMT sample prepared at 140 °C lacks a visible semicircle, showing instead an almost vertical low-frequency line, suggesting severely hindered faradic charge-transfer kinetics despite preserved capacitance behavior. For all urea-derived samples (Figure S11), the

Nyquist plots similarly show no semicircle, implying that charge-transfer processes are slow compared to ion diffusion and that electrode behavior is dominated by resistive and diffusive contributions.

When the two synthesis methods are compared, the HMTderived electrodes generally display more ideal pseudocapacitive behavior, with lower  $R_{ct}$  values, higher CPE exponents ( $\alpha$ ), and clearer separation between the semicircle and Warburg regions. The higher  $\alpha$  values in the HMT series (0.62–0.75) indicate a response closer to that of an ideal capacitor, consistent with a more open  $\alpha$ -Ni(OH)<sub>2</sub> layered structure and minimal carbonate incorporation at lower synthesis temperatures, which together enhance Ni2+ site accessibility and promote charge transfer. In the HMT series (Table S4), R<sub>ct</sub> is lowest at 80 °C (10.4  $\Omega$ ) and increases with synthesis temperature, peaking at 140 °C (89  $\Omega$ ), where the transformation to crystalline nickel carbonate hydroxide significantly restricts the accessibility of Ni2+ sites. The Warburg coefficient decreases sharply with temperature, and for the 120 and 140 °C samples, it becomes so small that the W element can be omitted from the equivalent circuit without degrading the fit, showing that ionic diffusion is no longer rate-limiting and that performance loss is governed by blocked Ni<sup>2+</sup> redox sites. In contrast, urea-derived samples exhibit lower  $\alpha$  values (Table S5), reflecting a greater deviation from ideal capacitive

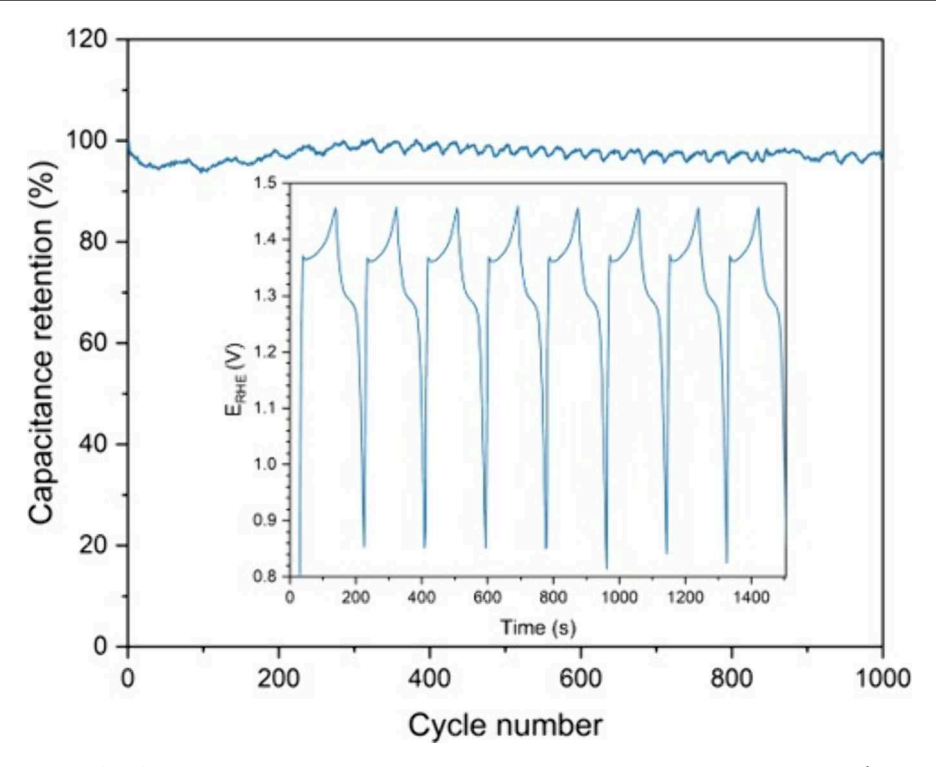


Figure 6. Cycling stability of  $Ni(OH)_2$ -H prepared at 80 °C measured in 1 M KOH at a current density of 1 A  $g^{-1}$  for 1000 cycles. Capacitance retention is plotted vs cycle number for 1000 consecutive GCD cycles, showing a capacitance retention of 92% after 1000 cycles. The inset shows GCD profiles for the first eight cycles.

behavior due to the higher carbonate content present at all synthesis temperatures. These samples lack a visible semicircle, display very high  $R_{\rm ct}$  values that increase from 103  $\Omega$  at 80 °C to 321  $\Omega$  at 140 °C, and show negligible Warburg contributions, confirming that the performance limitations arise primarily from restricted electrochemical access to Ni<sup>2+</sup> active sites rather than from slow ionic diffusion (i.e., the transport of ions through the electrolyte and into the active material).

3.3. In Situ X-ray Absorption Spectroscopy. To understand the enhanced pseudocapacitive behavior and the availability of Ni<sup>2+</sup> sites for electrochemical oxidation, we used in situ Ni K-edge XANES (X-ray absorption near-edge structure) analysis to directly monitor the Ni valence state in Ni(OH)<sub>2</sub>-H prepared by HMT decomposition at 80 °C during electrochemical charging and discharging. The Ni K-edge XANES spectra measured on as-prepared Ni(OH)2-H and on Ni(OH)<sub>2</sub>-H during electrochemical charging at OCP, 1.20, 1.30, 1.40, 1.45, 1.50, and 1.55 V versus RHE and during discharging at 1.30 and 1.00 V versus RHE are shown in Figure 7. For comparison, the Ni K-edge XANES spectra of the reference Ni compounds are added for comparison: commercial Ni oxide and Ni hydroxide, and a model Ni(OH)<sub>2</sub> catalyst for the oxygen evolution reaction 19 measured at OCP, as references for Ni<sup>2+</sup>, and the model Ni(OH)<sub>2</sub> catalyst measured at 1.7 V versus RHE during the OER, as a reference for Ni<sup>3.5+</sup>.

The Ni K edge shifts to a higher energy with an increase in the Ni valence state, as demonstrated in the operando Ni K-edge XANES experiment during charging of the NMC523 battery. A shift of the Ni K-edge position of 2.1 eV per valence state was found. In case of the model Ni(OH)<sub>2</sub> catalyst for the OER, presented in our previous work, the shift in the Ni K-edge position between the Ni(OH)<sub>2</sub> at the OCP, where

the Ni valence is +2.0, and Ni(OH)<sub>2</sub> at 1.70 V versus RHE during the OER is 3.1 eV (Figure 7). From the observed edge shift, we estimate that the average Ni valence in Ni(OH)<sub>2</sub> at 1.70 V is +3.5 ( $\pm$ 0.1), which is in good agreement with a theoretical estimation of the maximum average Ni valence in the range from +3.5 to +3.7 for the nickel hydroxide, which can be achieved during the OER.<sup>7</sup>

Principal component analysis (PCA) of the operando Ni XANES spectra of Ni(OH)<sub>2</sub>-H measured during electrochemical charging and discharging shows that a linear combination of two different components is sufficient to completely describe each XANES spectrum in the series. The linear combination fit (LCF) analysis shows that a linear combination of the XANES profiles of Ni(OH)<sub>2</sub>-H at the OCP and model Ni(OH)<sub>2</sub> OER catalyst at 1.70 V can completely describe the XANES spectra of all of the samples in the series. The goodness of the LCF fit is illustrated in Figure 8 for the XANES spectra of Ni(OH)<sub>2</sub>-H at 1.55 V during charging and Ni(OH)<sub>2</sub>-H at 1.30 V during discharging. The complete results of the LCF analysis are listed in Table 1.

LCF analysis provides information about the average Ni oxidation state during charging and discharging (Table 1). The Ni K-edge energy position in Ni(OH)<sub>2</sub>-H at the OCP is the same as in model Ni(OH)<sub>2</sub> at the OCP, where the Ni valence is  $\pm 2.0$ , so we can conclude that the average Ni valence in Ni(OH)<sub>2</sub>-H at the OCP is  $\pm 2.0$ . The Ni valence state increases during the electrochemical oxidation with an onset of Ni<sup>2+</sup>/Ni<sup>3+</sup> oxidation at about 1.30 V. No significant increase in the Ni valence is observed at lower potentials. The average valence of Ni in fully charged Ni(OH)<sub>2</sub>-H at 1.55 V versus RHE is  $\pm 3.0$  ( $\pm 0.1$ ). Upon discharge, the XANES spectra show satisfactory reversibility of Ni redox processes.

The Ni K-edge EXAFS analysis (see the Supporting Information for detailed information on modeling the

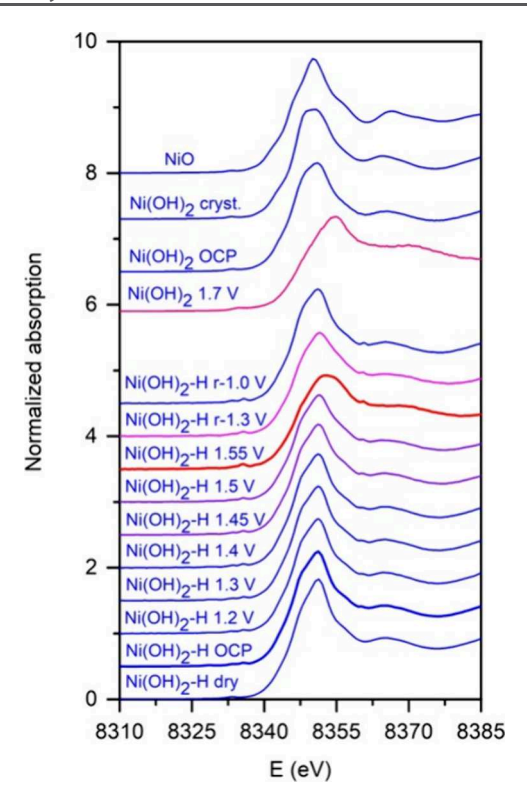


**Figure** 7. Normalized Ni K-edge XANES spectra of Ni(OH)<sub>2</sub>-H (prepared at 80 °C) measured on the dried powder (as prepared) and *in situ* during charging at the OCP, 1.20, 1.30, 1.40, 1.45, 1.50, and 1.55 V versus RHE and during discharging at 1.30 and 1.00 V vs RHE in the 1 M KOH electrolyte. Reference spectra are included for comparison: commercial NiO and Ni(OH)<sub>2</sub> powders, a model Ni(OH)<sub>2</sub> catalyst for the oxygen evolution reaction at OCP (representative of Ni<sup>2+</sup>), and the same catalyst at 1.7 V vs RHE (representative for Ni<sup>3.5+</sup>). All spectra were normalized to the edge step, energy-calibrated to a Ni metal foil reference, and vertically offset for the sake of clarity.

EXAFS spectra) shows that the average local structure around Ni cations changes upon charging of Ni(OH)<sub>2</sub> (Figure 9). For as-prepared Ni(OH)2-H measured as dried powder (Table S7), the Ni<sup>2+</sup> cations are coordinated with six oxygen neighbors in the first coordination shell at 2.05 Å and six Ni neighbors in the second coordination shell at 3.10 Å. At the OCP, hydrated Ni(OH)2-H experiences a deformation of coordination octahedra (Table S7). The first coordination shell is split into 1 + 5 coordination with one oxygen at 1.77 Å and five oxygens at 2.03 Å. The second coordination sphere has noe Ni at 2.96 Å and five at 3.10 Å. The shortening of one Ni-O distance can be explained by noncooperative Jahn-Teller distortion. Hydration with alkaline metal hydroxides causes the reorganization of hydrogen bonding between layers in the double hydroxide, resulting in the shrinkage of the unit cell parameter in the c-direction,<sup>6</sup> which is reflected in the Ni–O bond distances observed in the Ni K-edge EXAFS spectra. 29,30 The local structure of Ni(OH)2-H changes significantly in a fully charged state (1.55 V vs RHE) under in situ electrochemical conditions (Table S7). The Ni-O distance for the three nearest oxygens and the four shortest Ni-Ni distances are shorter than those in the as-prepared state. This agrees with XANES results, which show that the average Ni valence after full charging is oxidized to about +3 and, consequently, the interatomic distances to the nearest neighbors are shortened.<sup>31</sup>

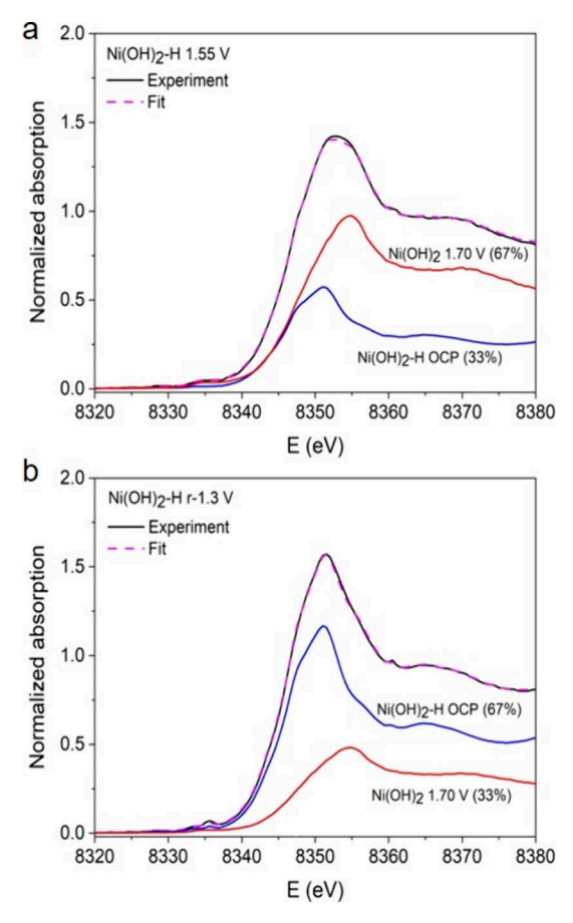


**Figure 8.** LCA fits of Ni K-edge XANES spectra for Ni(OH)<sub>2</sub>-H measured *in situ* in a 1 M KOH electrolyte at two electrochemical potentials: (a) at 1.55 V vs RHE during charging and (b) at 1.30 V vs RHE during discharging. In each panel, the black solid line is the experimental spectrum; the magenta dashed line is the best fit LCA result obtained from the reference spectra of Ni(OH)<sub>2</sub>-H at the OCP (representing Ni<sup>2+</sup>) and model Ni(OH)<sub>2</sub> OER catalyst at 1.70 V (representing Ni<sup>3.5+</sup>). For panel a, the fit corresponds to 33% Ni<sup>2+</sup> and 67% Ni<sup>3.5+</sup>, and for panel b, the fit corresponds to 67% Ni<sup>2+</sup> and 33% Ni<sup>3.5+</sup>.

Table 1. Average Ni Valences during Charging and Discharging of Ni(OH)<sub>2</sub>-H Prepared Using HMT at 80 °C Obtained by LCF Analysis of *In Situ* Ni K-Edge XANES Spectra Recorded in 1 M KOH<sup>a</sup>

potential (V vs RHE)	Ref1 Ni <sup>2+</sup>	Ref2 Ni <sup>3.5+</sup>	average Ni valence (error $\pm$ 0.1)
Charging			
OCP	100%	0%	+2.00
1.20	100%	0%	+2.00
1.30	98%	2%	+2.03
1.40	96%	4%	+2.06
1.45	87%	13%	+2.20
1.50	77%	23%	+2.35
1.55	33%	67%	+3.00
Discharging			
1.30	67%	33%	+2.50
1.00	98%	2%	+2.03

<sup>a</sup>The fits used the XANES spectrum of Ni(OH)<sub>2</sub>-H at the OCP as a reference for Ni<sup>2+</sup> (Ref1) and model Ni(OH)<sub>2</sub> OER catalyst at 1.70 V as a reference for Ni<sup>3.5+</sup> (Ref2).

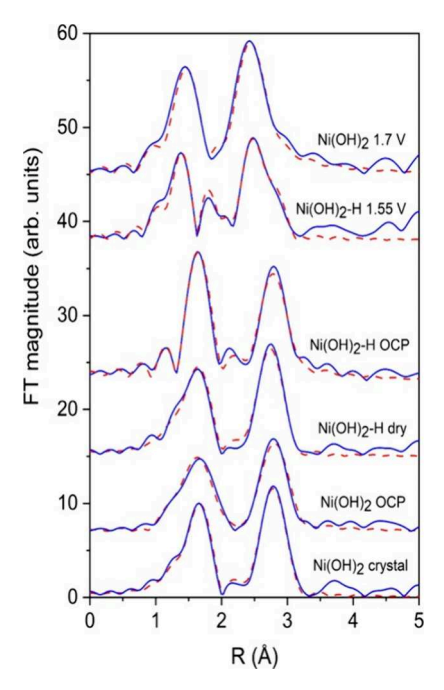


**Figure 9.** Fourier transform magnitude of  $k^3$ -weighted Ni K-edge EXAFS spectra of Ni(OH)<sub>2</sub>-H (prepared at 80 °C) measured on the dried powder (as prepared) and *in situ* during electrochemical charging at the OCP and at 1.55 V vs RHE in a 1 M KOH electrolyte. The Fourier transforms were calculated over the k range of 3-13 Å $^{-1}$ , and the best fit EXAFS model (red dashed line) was obtained by fitting over the k range of 1.1-3.2 Å to experimental data (blue solid line). Reference spectra are included for comparison: commercial Ni(OH)<sub>2</sub> powder and a model Ni(OH)<sub>2</sub> OER catalyst at OCP (representative Ni<sup>2+</sup>) and the same catalyst at 1.7 V vs RHE (representative Ni<sup>3.5+</sup>). Spectra are vertically offset for the sake of clarity.

A similar octahedral deformation is observed around Ni cations in the model Ni(OH)<sub>2</sub> OER catalyst, where at the OCP (Figure 9 and Table S6), the first coordination shell contains one oxygen at 1.67 Å and five at 2.08 Å and the second coordination shell contains five Ni atoms at 3.13 Å and one at 3.25 Å. In the OER region at 1.70 V versus RHE (Figure 9 and Table S6), some of the Ni–O and Ni–Ni distances are significantly decreased. Compared to the Ni(OH)<sub>2</sub>-H charged at 1.55 V versus RHE, the number of neighboring atoms with shorter distances is increased. On average, 4.8 oxygens are at a shorter distance at the OER compared to 3.0 for charged Ni(OH)<sub>2</sub>-H. This follows XANES data, showing more oxidized Ni during the OER.

# 4. CONCLUSIONS

This work demonstrates that the incorporation of carbonate species has a pronounced impact on the electrochemical performance of the Ni(OH)<sub>2</sub> materials synthesized using HMT and urea precipitating agents. At lower temperatures (80 and 100 °C), partial decomposition of HMT leads to the formation of a less ordered  $\alpha$ -phase with expanded interlayer spacing, allowing for greater ion accessibility and resulting in enhanced capacitance. In contrast, higher synthesis temperatures (120 and 140 °C) promote complete HMT decomposition and the incorporation of carbonate ions into the crystal lattice, forming a more compact and crystalline structure that limits the mobility of electrolyte ions and restricts access to Ni<sup>2+</sup> redox sites, thereby diminishing

capacitance and energy density. Regardless of the synthesis temperature, urea-based samples result in poor electrochemical performance. Even at lower temperatures, the urea decomposition process introduces carbonate species that integrate into the structure, reducing the accessibility of redox-active Ni<sup>2+</sup> sites. At higher temperatures, the samples crystallize into nickel carbonate hydroxide phases, further reducing the capacitance values. To the best of our knowledge, this is the first systematic study to demonstrate that carbonate incorporation directly governs both the structural evolution and the pseudocapacitive performance of Ni(OH)<sub>2</sub> synthesized from HMT versus urea. These insights establish a framework that can be extended to other layered transition metal hydroxides prepared hydrothermally.

# ASSOCIATED CONTENT

# Supporting Information

The Supporting Information is available free of charge at https://pubs.acs.org/doi/10.1021/acs.chemmater.5c01467.

Summary of capacitances for Ni(OH)<sub>2</sub> pseudocapacitors with different morphologies; TGA-MS curves of Ni-(OH)<sub>2</sub>-H and Ni(OH)<sub>2</sub>-U prepared at different temperatures; Raman spectra of Ni(OH)<sub>2</sub>-H and Ni(OH)<sub>2</sub>-U samples prepared at different temperatures; FTIR spectra of Ni(OH)<sub>2</sub>-H and Ni(OH)<sub>2</sub>-U prepared at different temperatures; summary of the specific surface area obtained from N2 physisorption analysis for Ni(OH)<sub>2</sub>-H and Ni(OH)<sub>2</sub>-U samples synthesized at different temperatures; pore size distribution of Ni-(OH)<sub>2</sub>-H and Ni(OH)<sub>2</sub>-U samples prepared at different temperatures; comparison of the cyclic voltammograms, charge-discharge curves, and calculated capacitances for Ni(OH)<sub>2</sub>-H and Ni(OH)<sub>2</sub>-U samples prepared at 80 °C; electrochemical impedance spectroscopy (EIS) curves of Ni(OH)<sub>2</sub>-H and Ni(OH)<sub>2</sub>-U samples prepared at different temperatures; and details of EXAFS analysis and best fit parameters of nearest coordination shells around Ni in the commercial Ni hydroxide, the model Ni(OH)<sub>2</sub> catalyst for OER at OCP and at 1.7 V versus RHE, and Ni(OH)2-H as prepared dried powder at OCP and 1.55 V versus RHE (PDF)

# AUTHOR INFORMATION

#### **Corresponding Author**

Andraž Mavrič — University of Nova Gorica, SI-5000 Nova Gorica, Slovenia; orcid.org/0000-0003-2017-9880; Email: andraz.mavric@ung.si

## **Authors**

Anja Siher — University of Nova Gorica, SI-5000 Nova Gorica, Slovenia

Ksenija Maver – University of Nova Gorica, SI-5000 Nova Gorica, Slovenia; National Institute of Chemistry, SI-1001 Ljubljana, Slovenia

Iztok Arčon — University of Nova Gorica, SI-5000 Nova Gorica, Slovenia; Jožef Stefan Institute, SI-1000 Ljubljana, Slovenia; o orcid.org/0000-0003-4333-4054

Complete contact information is available at: https://pubs.acs.org/10.1021/acs.chemmater.5c01467

#### **Author Contributions**

Conceptualization: A.M. Data curation: A.S. Formal analysis: A.S., K.M., I.A., and A.M. Investigation: A.S., K.M., I.A., and A.M. Methodology: A.S., I.A., and A.M. Resources: A.S. and A.M. Supervision: A.M. Validation: A.S., K.M., I.A., and A.M. Visualization: A.S., I.A., and A.M. Writing of the original draft: A.S. Review and editing: I.A. and A.M.

#### Notes

The authors declare no competing financial interest.

# ACKNOWLEDGMENTS

This work was supported by the Slovenian Research and Innovation Agency (Research Core Funding P2-0412, P1-0112, and P1-0418 and Projects J2-50058, J1-50220, and J7-4636). The authors acknowledge DESY, a member of the Helmholtz Association HGF, for the provision of experimental facilities. Parts of this research were carried out at PETRA III, and the authors thank P65 beamline staff Edmund Welter, Sergiu Levcenco, and Tinku Dan for their support during the XAFS experiment. Beamtime was allocated for Proposals I-20230893 EC and I-20240152 EC.

## REFERENCES

- (1) Sharma, S.; Kadyan, P.; Sharma, R. K.; Kumar, N.; Grover, S. Progressive Updates on Nickel Hydroxide and Its Nanocomposite for Electrochemical Electrode Material in Asymmetric Supercapacitor Device. *Journal of Energy Storage* **2024**, *87*, 111368.
- (2) Simon, P.; Gogotsi, Y. Perspectives for Electrochemical Capacitors and Related Devices. *Nat. Mater.* **2020**, *19* (11), 1151–1163.
- (3) Aricò, A. S.; Bruce, P.; Scrosati, B.; Tarascon, J.-M.; Van Schalkwijk, W. Nanostructured Materials for Advanced Energy Conversion and Storage Devices. *Nat. Mater.* **2005**, *4* (5), 366–377.
- (4) Wang, Y.; Song, Y.; Xia, Y. Electrochemical Capacitors: Mechanism, Materials, Systems, Characterization and Applications. *Chem. Soc. Rev.* **2016**, *45* (21), 5925–5950.
- (5) Liu, R.; Zhou, A.; Zhang, X.; Mu, J.; Che, H.; Wang, Y.; Wang, T.-T.; Zhang, Z.; Kou, Z. Fundamentals, Advances and Challenges of Transition Metal Compounds-Based Supercapacitors. *Chemical Engineering Journal* **2021**, *412*, 128611.
- (6) Hall, D. S.; Lockwood, D. J.; Bock, C.; MacDougall, B. R. Nickel Hydroxides and Related Materials: A Review of Their Structures, Synthesis and Properties. *Proc. R. Soc. A* **2015**, *471* (2174), 20140792.
- (7) Yi, X.; Sun, H.; Robertson, N.; Kirk, C. Nanoflower Ni(OH)<sub>2</sub> Grown in Situ on Ni Foam for High-Performance Supercapacitor Electrode Materials. Sustainable Energy Fuels **2021**, 5 (20), 5236–5246.
- (8) Akhtar, M. S.; Wejrzanowski, T.; Komorowska, G.; Adamczyk-Cieślak, B.; Choinska, E. Microwave-Assisted Hydrothermal Synthesis of  $\alpha\beta$ -Ni(OH)<sub>2</sub> Nanoflowers on Nickel Foam for Ultra-Stable Electrodes of Supercapacitors. *Electrochim. Acta* **2024**, *508*, 145284.
- (9) Yufanyi, D. M.; Ndibewu, P. P.; Heveling, J. Hexamethylenetetramine-Precipitated α-Ni(OH)<sub>2</sub> as Precursors for NiO Nanoparticles: Structural and Morphological Characterization. *J. Nanosci Nanotechnol.* **2015**, *15* (9), 6818–6825.
- (10) Cheng, M.-Y.; Hwang, B.-J. Control of Uniform Nanostructured  $\alpha$ -Ni(OH)<sub>2</sub> with Self-Assembly Sodium Dodecyl Sulfate Templates. *J. Colloid Interface Sci.* **2009**, 337 (1), 265–271.
- (11) Sarfraz, M.; Shakir, I. Recent Advances in Layered Double Hydroxides as Electrode Materials for High-Performance Electrochemical Energy Storage Devices. *Journal of Energy Storage* **2017**, *13*, 103–122.
- (12) Bukhtiyarova, M. V. A Review on Effect of Synthesis Conditions on the Formation of Layered Double Hydroxides. *J. Solid State Chem.* **2019**, 269, 494–506.

- (13) He, J.; Wei, M.; Li, B.; Kang, Y.; Evans, D. G.; Duan, X. Preparation of Layered Double Hydroxides. In *Layered Double Hydroxides*; Duan, X., Evans, D. G., Eds.; Springer: Berlin, 2006; pp 89–119.
- (14) Ma, Y.; Yang, M.; Jin, X. Formation Mechanisms for Hierarchical Nickel Hydroxide Microstructures Hydrothermally Prepared with Different Nickel Salt Precursors. *Colloids Surf., A* **2020**, 588, 124374.
- (15) Siher, A.; Maver, K.; Luin, U.; Pintar, A.; Arčon, I.; Mavrič, A. Beyond Surface Area: Enhanced Pseudocapacitive Properties of Cobalt Layered Double Hydroxide through Structural Modifications. Surfaces and Interfaces 2025, 62, 106174.
- (16) Ravel, B.; Newville, M. ATHENA, ARTEMIS, HEPHAESTUS: Data Analysis for X-Ray Absorption Spectroscopy Using IFEFFIT. J. Synchrotron Rad 2005, 12 (4), 537–541.
- (17) Glemser, O.; Einerhand, J. Die Struktur höherer Nickelhydroxyde. Z. Anorg. Chem. **1950**, 261 (1–2), 43–51.
- (18) Rincke, C.; Bette, S.; Dinnebier, R. E.; Voigt, W. Nickel Bicarbonate Revealed as a Basic Carbonate. *Eur. J. Inorg. Chem.* **2015**, 2015 (36), 5913–5920.
- (19) Mavric, A.; Fanetti, M.; Lin, Y.; Valant, M.; Cui, C. Spectroelectrochemical Tracking of Nickel Hydroxide Reveals Its Irreversible Redox States upon Operation at High Current Density. *ACS Catal.* **2020**, *10* (16), 9451–9457.
- (20) Dufresne, W. J. B.; Rufledt, C. J.; Marshall, C. P. Raman Spectroscopy of the Eight Natural Carbonate Minerals of Calcite Structure. *J. Raman Spectrosc.* **2018**, 49 (12), 1999–2007.
- (21) Hollingbery, L. A.; Hull, T. R. The Thermal Decomposition of Huntite and Hydromagnesite—A Review. *Thermochim. Acta* **2010**, 509 (1–2), 1–11.
- (22) Matsuda, K.; Okuda, A.; Iio, N.; Tarutani, N.; Katagiri, K.; Inumaru, K. Chemical and Structural Transformations of M -Al-CO<sub>3</sub> Layered Double Hydroxides (M = Mg, Zn, or Co, M/Al = 2) at Elevated Temperatures: Quantitative Descriptions and Effect of Divalent Cations. *Inorg. Chem.* **2024**, *63* (34), 15634–15647.
- (23) A, S.; T, B.; V, G.; D, S.; Kulal, N.; A, S. Framework of Ruthenium-Containing Nickel Hydrotalcite-Type Material: Preparation, Characterisation, and Its Catalytic Application. *RSC Adv.* **2018**, 8 (44), 25248–25257.
- (24) Rey, C.; Renugopalakrishman, V.; Collins, B.; Glimcher, M. J. Fourier Transform Infrared Spectroscopic Study of the Carbonate Ions in Bone Mineral during Aging. *Calcif. Tissue Int.* **1991**, 49 (4), 251–258
- (25) Balaji, T. E.; Tanaya Das, H.; Maiyalagan, T. Recent Trends in Bimetallic Oxides and Their Composites as Electrode Materials for Supercapacitor Applications. *ChemElectroChem.* **2021**, 8 (10), 1723–1746
- (26) Dang, L.; Liang, H.; Zhuo, J.; Lamb, B. K.; Sheng, H.; Yang, Y.; Jin, S. Direct Synthesis and Anion Exchange of Noncarbonate-Intercalated NiFe-Layered Double Hydroxides and the Influence on Electrocatalysis. *Chem. Mater.* **2018**, *30* (13), 4321–4330.
- (27) Qu, D.; Wang, G.; Kafle, J.; Harris, J.; Crain, L.; Jin, Z.; Zheng, D. Electrochemical Impedance and Its Applications in Energy-Storage Systems. *Small Methods* **2018**, 2 (8), 1700342.
- (28) Ohnuma, T.; Kobayashi, T. X-Ray Absorption near Edge Structure Simulation of LiNi<sub>0.5</sub>Co<sub>0.2</sub>Mn<sub>0.3</sub>O<sub>2</sub> *via* First-Principles Calculation. *RSC Adv.* **2019**, *9* (61), 35655–35661.
- (29) Yi, X.; Celorrio, V.; Zhang, H.; Robertson, N.; Kirk, C.  $\alpha/\beta$ -Ni(OH)<sub>2</sub> Phase Control by F-Ion Incorporation to Optimise Hybrid Supercapacitor Performance. *J. Mater. Chem. A* **2023**, *11* (41), 22275–22287.
- (30) Pandya, K. I.; et al. Extended X-ray Absorption Fine Structure Investigations of Nickel Hydroxides. *J. Phys. Chem.* **1990**, 94 (1), 21–26.
- (31) Pang, W. K.; Kalluri, S.; Peterson, V. K.; Dou, S. X.; Guo, Z. Electrochemistry and Structure of the Cobalt-Free  $\rm Li_{1+x}$  MO<sub>2</sub> (M = Li, Ni, Mn, Fe) Composite Cathode. *Phys. Chem. Chem. Phys.* **2014**, 16 (46), 25377–25385.